Geophysical Prospecting

Geophysical Prospecting

ORIGINAL ARTICLE OPEN ACCESS

Application of Neural Networks for Moon Near-Surface Velocity-Model Extraction

Nelson Ricardo Coelho Flores Zuniga[1] | Deyan Draganov[2]

[1]Instituto do Mar, Universidade Federal de São Paulo, São Paulo, Brazil | [2]Faculty of Civil Engineering and Geosciences, Delft University of Technology, Delft, the Netherlands

Correspondence: Nelson Ricardo Coelho Flores Zuniga (zuniga@unifesp.br)

Received: 10 January 2026 | **Revised:** 21 May 2026 | **Accepted:** 25 May 2026

Keywords: machine learning | Moon | near-surface | neural network | spectral recomposition

ABSTRACT

Characterizing the shallow lunar subsurface is essential for future exploration activities, including landing-site assessment, infrastructure construction and subsurface resource investigation. However, conventional seismic approaches for near-surface characterization commonly depend on prior velocity information and assumptions regarding the geological structure, which are difficult to constrain for legacy Apollo seismic datasets acquired with unconventional geometries. In this study, we propose a data-driven methodology integrating spectral recomposition and neural networks (NNs) for lunar near-surface velocity-model prediction using active-source seismic data acquired during the Apollo missions. The proposed approach reconstructs spectral information associated with seismic wavelets linked to reflected events and incorporates this information as an additional feature for training a fully convolutional NN. To accommodate the Apollo acquisition geometry, the seismic traces were reorganized into combined common-receiver gathers. Synthetic datasets representative of expected lunar near-surface formations, including unconsolidated regolith and underlying consolidated layers, were generated to train the network. The predicted velocity models successfully reproduced the main kinematic characteristics observed in the lunar seismic data, including continuity of reflected events and travel-time trends. Forward modelling using the reconstructed models generated synthetic seismograms consistent with the observed Apollo seismic data, yielding low normalized root-mean-square error values. The results indicate the presence of a shallow low-velocity regolith layer overlying a more consolidated unit, consistent with previous Apollo 16 and Apollo 17 studies. These findings demonstrate that the proposed methodology can provide physically consistent lunar near-surface velocity models directly from seismic data, without requiring prior velocity analysis, highlighting its potential for future planetary seismic exploration and lunar geotechnical investigations.

1 | Introduction

Seismic studies are essential in investigating and characterizing near-surface geological structures, which are crucial for understanding planetary surfaces, including the Moon. On Earth, near-surface seismic imaging has been widely applied in environmental studies, geotechnical investigations, groundwater exploration and engineering site characterization (e.g., Zuniga et al. 2023a, 2023b). However, the challenge of extracting valuable information from seismic data—such as signal parameters and accurate prediction of near-surface features—might become even more challenging when applied to extraterrestrial environments due to factors such as lower gravity and the lack of atmosphere, which results in lower seismic attenuation compared to Earth. This condition affects signal behaviour and interpretation but also enables improved temporal separation of reflection events.

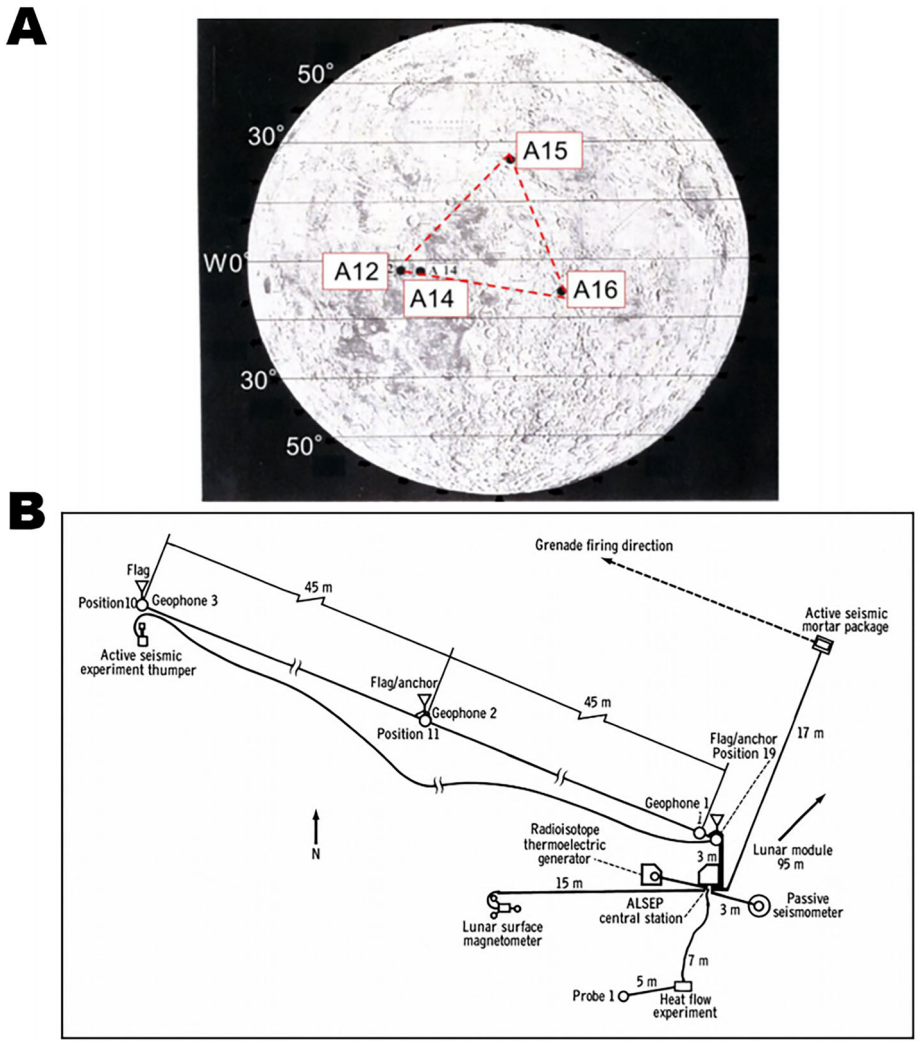

FIGURE 1 | (A) Apollo Passive Seismic Experiment Network—A16 indicates the Apollo 16 mission location site. (B) Deployment configuration for Apollo 16 experiment (adapted from NASA TM X-58131 1974).

Unlike terrestrial sediments, the lunar regolith is completely dry and highly porous and therefore does not exhibit moisture-related or atmospheric attenuation. These unique subsurface properties include strongly unconsolidated regolith, a brecciated transition zone, and underlying coherent basaltic bedrock with significant acoustic impedance contrasts.

Understanding the geotechnical parameters of the lunar subsurface is of critical importance for future Moon exploration missions. Establishing permanent lunar stations in underground structures—such as lava tunnels—could provide essential protection for personnel against solar radiation and micrometeorite impacts. Estimating the subsurface parameters with minimal intrusion is possible through seismic methods, as demonstrated in previous studies using both passive and active seismic sources. The Apollo 16 acquisition geometry and experiment configuration are illustrated in Figure 1. Cooper et al. (1974) and Heffels et al. (2021) applied active-source seismic refraction methods to estimate P-wave velocities. Larose et al. (2005) used passive sources and seismic interferometry to retrieve surface waves and invert them for S-wave velocity estimates. Nishitsuji et al. (2016), Nishitsuji et al. (2020) and Imazato et al. (2023) applied seismic interferometry to deep moonquakes and active-source Apollo data to estimate subsurface structures and azimuthal anisotropy. However, techniques such as critical angle (CA) detection and phase-shift estimation, successfully applied to Earth-based datasets (Zuniga et al. 2023a, 2023b), show promising results for analysing unconsolidated lunar materials.

In recent years, neural networks (NNs) have become an effective tool for extracting information from seismic data, enabling the identification of subsurface patterns and improving imaging in complex environments (Jia and Ma 2017; Jia et al. 2018; Zhang et al. 2019). Leveraging the power of deep learning, NNs have emerged as a robust tool for fast extraction of essential insights from seismic data (Ren et al. 2020). These networks can autonomously learn intricate patterns and relationships within subsurface structures by analysing large volumes of seismic data, enabling highly accurate and efficient imaging (Wrona et al. 2018; Jia et al. 2018). The ability of NNs to recognize seismic features and distinguish signal from noise significantly enhances the quality of near-surface seismic images, supporting precise identification of geological features such as stratigraphic layering, fractures and buried channels (e.g., Di et al. 2019; Klochikhina

et al. 2020). This synergy between seismic imaging and NN technology represents a substantial advancement in planetary near-surface seismic exploration. Seismic attributes and data-driven approaches have also been widely applied for subsurface characterization and feature detection in complex environments (Ismail et al. 2020, 2021, 2022; Gammaldi et al. 2022).

In this study, we propose a data-driven framework that combines spectral recomposition (SR) with a fully convolutional network (FCN) to improve near-surface seismic velocity prediction in the lunar subsurface. The approach integrates spectral information extracted from seismic data with deep learning techniques to enhance the characterization of shallow geological structures. This combination enables a more effective use of limited and noisy seismic datasets, such as those acquired during the Apollo missions.

The proposed approach aims to improve the prediction of near-surface lunar features under constrained acquisition conditions, including regolith thickness variations and shallow subsurface structures. The lunar near-surface presents significant challenges, such as high heterogeneity, unconsolidated materials and the absence of fluid saturation, which affect seismic wave propagation. By integrating SR with a data-driven framework, this study seeks to enhance the characterization of these complex environments using limited and noisy seismic data.

The SR–FCN framework adopted in this study has been previously validated using controlled synthetic experiments, including benchmark models such as Marmousi II (Zuniga 2024, 2026a), which are widely used to assess seismic imaging and inversion methods under complex geological conditions. The same framework was also successfully applied to near-surface seismic data (Zuniga 2026b). These studies demonstrated the robustness of the approach in the presence of strong lateral heterogeneities.

In this work, we extend the application of this validated framework to real lunar seismic data acquired during the Apollo missions, evaluating its capability to improve near-surface velocity characterization under constrained acquisition conditions through a data-driven approach. The training dataset is constructed based on prior 1D stratified models derived from previous Apollo studies. However, the proposed SR–FCN workflow enables the prediction of laterally varying (2D) velocity structures, extending these simplified models into more realistic representations of the lunar near-surface.

Although the proposed framework enables the prediction of laterally varying velocity structures, it is important to emphasize that the present study is primarily focused on evaluating the capability of the SR–FCN workflow under constrained acquisition conditions. The application to Apollo 16 data should therefore be interpreted as a data-driven reconstruction guided by seismic responses, rather than as a fully validated geological model of lateral heterogeneity.

2 | Theory

2.1 | SR Method

SR is a signal-processing approach based on the decomposition and reconstruction of seismic waveforms in the frequency domain (Huang et al. 1998; Castagna et al. 2003; Li et al. 2011; Cai et al. 2013). In this study, SR is used to estimate wavelet attributes including amplitude, peak frequency and phase.

The implementation adopted in this work follows the inversion-based SR framework proposed by Zuniga et al. (2023a, 2023b) and Zuniga and Priimenko (2024, 2025), in which seismic traces are decomposed into constituent wavelets to enhance spectral and temporal localization. The SR process reconstructs amplitude, phase and arrival-time attributes in the frequency domain using short-time Fourier transform (STFT) analysis followed by spectral-ratio inversion (Tomasso et al. 2010; Cai et al. 2013):

$$d(f) \approx \sum_{i=1}^{n} R_i(m_i, f). \tag{1}$$

where $R_i(m_i, f)$ represents the spectrum of the ith Ricker-wavelet component. Each component is defined as

$$R_i(m_i, f) = a_i \, \psi(m_i, f), \tag{2}$$

where a_i denotes the amplitude and m_i the peak frequency of the wavelet component. The adopted Ricker spectral representation is expressed as

$$\psi(m_i, f) = \frac{f^2}{{m_i}^2} \exp\left\{ -\frac{f^2}{{m_i}^2} \right\}. \tag{3}$$

The inversion procedure is formulated as a least-squares optimization problem in which the reconstructed spectrum is fitted to the observed spectrum by minimizing the residual error,

$$\min_{\mathbf{a},\mathbf{m}} \|\mathbf{r}(\mathbf{a}, \mathbf{m})\|_2^2. \tag{4}$$

where $\mathbf{r}(\mathbf{a}, \mathbf{m})$ denotes the residual between the observed and reconstructed spectra as a function of the recovered amplitudes and peak frequencies.

The adopted Ricker-wavelet representation provides a parametric approximation of localized seismic wavelets. In field data such as the Apollo 16 records, deviations from an ideal Ricker wavelet may arise due to instrument response, digitization effects, attenuation and non-stationary source characteristics. Within the SR inversion, the Ricker model is used to approximate the dominant spectral behaviour of localized wavelets rather than to reproduce the exact physical waveform. Consequently, the extracted attributes represent the effective spectral and temporal characteristics of the seismic signal.

The SR-based analysis does not explicitly separate primary reflections from multiple-related events and diffracted wavefields. Consequently, the extracted attributes represent the combined seismic response of the recorded wavefield.

2.2 | FCNs for Seismic Inversion

FCNs are deep learning models designed for dense pixel-wise prediction tasks, making them suitable for seismic inversion and subsurface imaging (Li et al. 2019; Adler et al. 2021; An et al. 2021).

Unlike traditional CNNs, FCNs replace fully connected layers with convolutional operations, preserving spatial information and enabling high-resolution output prediction.

In seismic applications, FCNs have demonstrated the capability to capture spatial and temporal patterns in seismic data, enabling direct mapping between seismic responses and subsurface physical properties (Li et al. 2019; Adler et al. 2021; An et al. 2021).

The architecture adopted in this study is inspired by the U-Net model (Ronneberger et al. 2015), which has been adapted for geophysical applications (Yang and Ma 2019). The U-Net structure follows an encoder–decoder paradigm, where the contracting path extracts hierarchical features from the input data, and the expanding path reconstructs spatial resolution through skip connections.

In geophysical applications, U-Net-based FCN architectures have been applied to seismic velocity-model prediction and inversion tasks (Yang and Ma 2019). Recent developments have explored the integration of seismic attributes into FCN frameworks, including SR-derived features. Previous studies (Zuniga 2024, 2026a, 2026b) showed that incorporating wavelet-based spectral and temporal attributes into FCN inputs improves prediction stability and reconstruction accuracy.

3 | Method

3.1 | Apollo 16 Data and Preprocessing

The dataset used in this study corresponds to the Apollo 16 active seismic experiment (ASE), consisting of thumper-source P-wave records acquired along a short-offset geophone array. The data were recorded at a sampling rate of approximately 530 Hz and digitized using a 5-bit logarithmic compression system. The acquisition system imposes limited dynamic range and reduced spectral resolution.

The experiment includes 19 shot locations, each recorded by three stationary geophones, yielding a total of 57 traces. Examples of Apollo 16 seismic records are shown in Figure 2. These data were reorganized into three common-receiver gathers (CRGs), each containing 19 traces. The CRGs were subsequently merged into a single combined CRG by aligning traces according to offset and removing redundant measurements. The resulting dataset contains 37 traces distributed over offsets ranging from approximately −91.44 to 91.44 m, as illustrated in Figure 3.

The preprocessing workflow included inspection for amplitude clipping and digitization artefacts associated with the acquisition system, median filtering for spike removal, spectral balancing, amplitude normalization, band-pass filtering (5–80 Hz) and segmentation into overlapping 0.5 s windows. Each trace was normalized by its maximum absolute amplitude within the analysis window. The complete preprocessing workflow applied to the Apollo 16 dataset is summarized in Figure 4.

The logarithmic compression associated with the 5-bit acquisition system implies that the recorded amplitudes do not correspond to

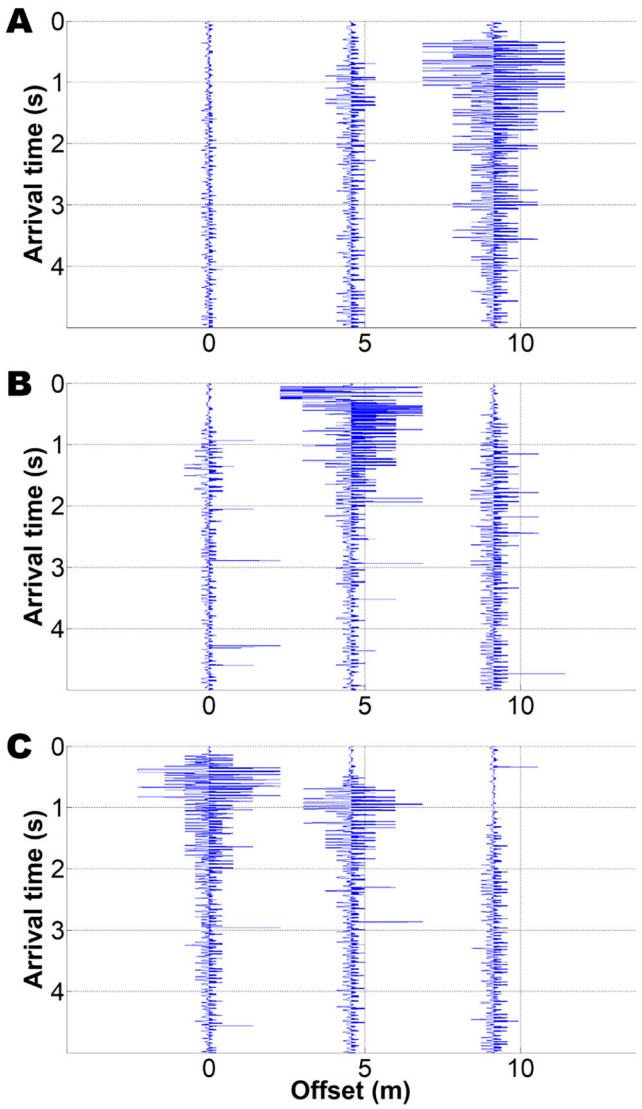

FIGURE 2 | Examples of shots obtained from Apollo 16 mission experiment: (A) shot 3, (B) shot 10 and (C) shot 17.

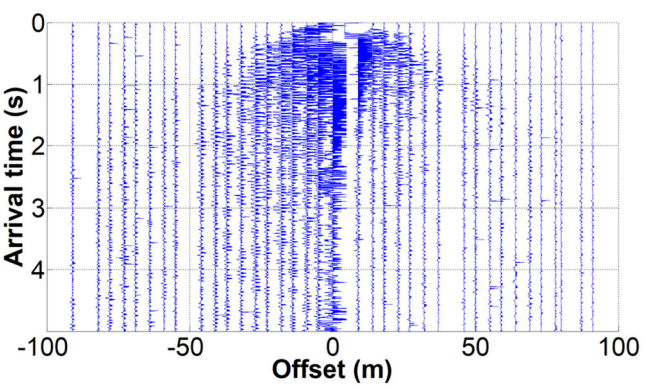

FIGURE 3 | Common-receiver gather (CRG) constructed by merging traces from multiple shot positions into a single combined common-receiver gathers after offset alignment. The resulting dataset contains 37 traces distributed between offsets of −91.44 and 91.44 m.

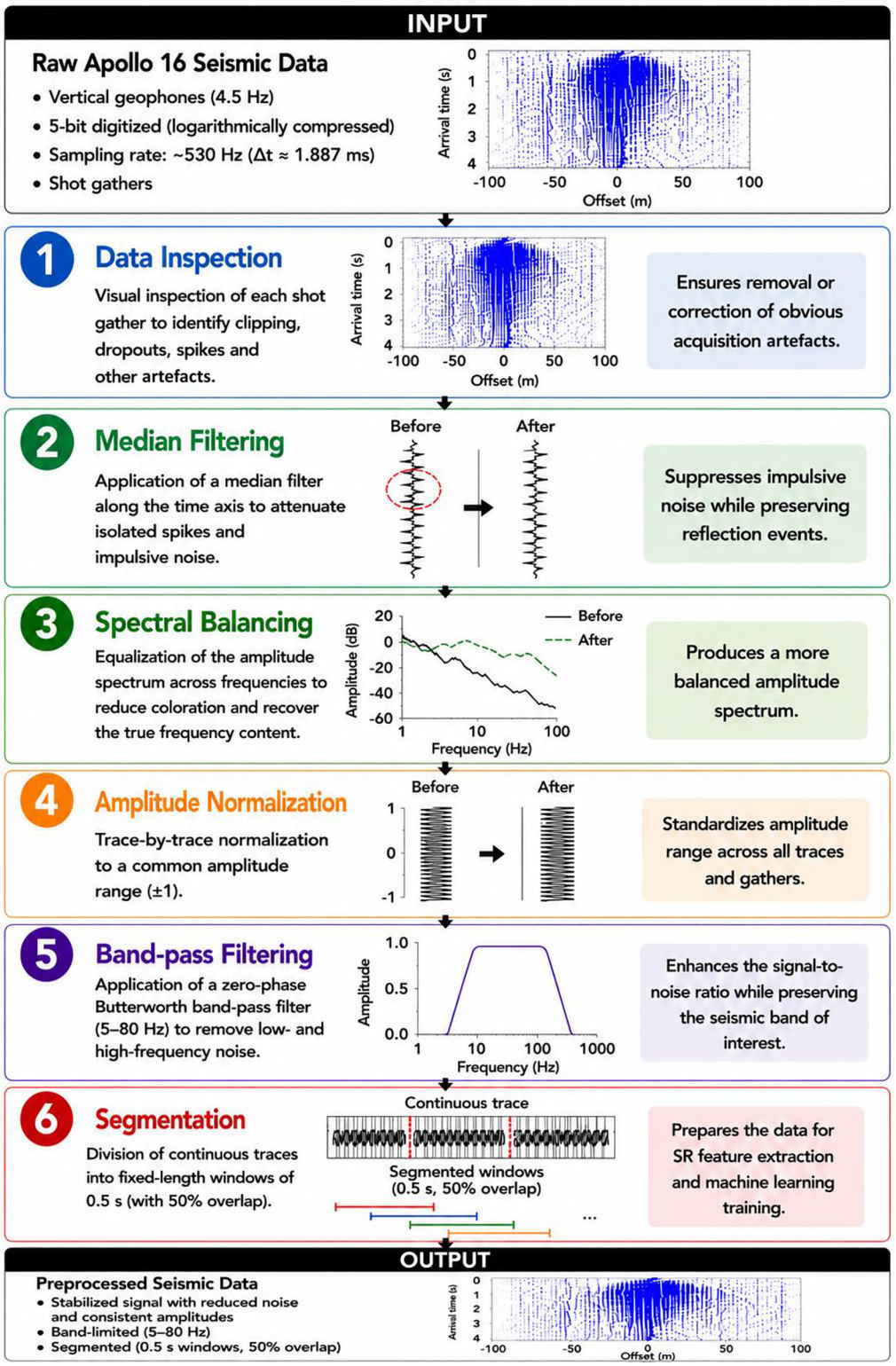

FIGURE 4 | Preprocessing workflow applied to the Apollo 16 seismic dataset. The pipeline includes data inspection for amplitude clipping and digitization artefacts, median filtering for spike removal, spectral balancing to equalize frequency content, amplitude normalization to standardize trace amplitudes, band-pass filtering (5–80 Hz) to suppress noise and segmentation into overlapping 0.5 s windows. These steps aim to stabilize the signal and preserve its spectral and temporal characteristics prior to spectral recomposition (SR)-based feature extraction.

a linear amplitude scale. No explicit decompression was applied in this study. Consequently, the analysis focuses primarily on relative spectral and temporal attributes, which are less sensitive to compression-related distortions (Wood 1974).

3.2 | Synthetic Models Generation

A total of 1000 synthetic near-surface models were generated using velocity and layer-thickness ranges consistent with Apollo 16 field conditions (Cooper et al. 1974; Sens-Schönfelder and Larose, 2010; Heffels et al. 2021).

The models were generated by randomly sampling layer thicknesses (2–10 m) and P-wave velocities (100–400 m/s) on the basis of values reported in previous lunar studies. Observed spectral ranges, signal-to-noise conditions and first-arrival travel times from the Apollo dataset were used to constrain the synthetic data generation.

Each model was forward simulated using a two-dimensional acoustic finite-difference scheme following Thorbecke and Draganov (2011), reproducing the acquisition geometry of the Apollo 16 dataset.

Forward modelling was performed using a two-dimensional acoustic finite-difference scheme. The computational grid consists of 300 × 200 samples (horizontal distance × depth), with spatial sampling intervals of approximately 0.612 m horizontally and 0.503 m in depth. The temporal discretization used a time step of $\Delta t = 1 \times 10^{-4}$ s, satisfying the Courant–Friedrichs–Lewy (CFL) stability condition for the maximum modelled velocity. The total simulation time was set to 1 s.

The finite-difference simulations were performed on a regular computational grid, whereas the Apollo 16 field data correspond to a non-uniform shot receiver geometry with 37 traces distributed over offsets ranging from approximately −91.44 to 91.44 m. Absorbing boundary conditions with sponge layers were applied along the model edges to attenuate artificial boundary reflections. The seismic source was represented by a Ricker wavelet with a central frequency of 20 Hz, consistent with the effective bandwidth of the Apollo 16 short-period seismic instruments. The source was injected as a point source in the pressure field.

Wave propagation was simulated using a second-order finite-difference formulation of the acoustic wave equation in time and space. The synthetic gathers were generated by sampling the modelled wavefield at receiver locations corresponding to the reconstructed Apollo acquisition geometry. The resulting synthetic traces were resampled to match the temporal sampling of the Apollo dataset ($\Delta t \approx 1.887 \times 10^{-3}$ s).

Noise and spectral characteristics consistent with the Apollo dataset, including signal-to-noise variations and bandwidth limitations, were incorporated into the synthetic gathers.

The Apollo 16 seismic data were used to constrain the synthetic training models through observed spectral ranges, signal-to-noise conditions and first-arrival travel times. Noise and bandwidth limitations consistent with the observed data were incorporated into the synthetic gathers to reproduce the acquisition characteristics of the Apollo dataset.

3.3 | SR-Based Feature Extraction

Following Tomasso et al. (2010), a seismic trace can be represented as a superposition of Ricker wavelets (Ricker 1953). Each wavelet is characterized by amplitude, peak frequency and phase attributes, which define the spectral representation of the seismic signal.

Isolated reflection events are extracted through temporal windowing and transformed into the frequency domain. A theoretical Ricker spectrum is fitted to the observed spectrum through least-squares inversion (Zuniga et al. 2023a). The inversion employs a multi-start optimization strategy (Sotirov and Terlaky 2013) initialized from multiple starting points, and the solution with the minimum spectral misfit is selected. This inversion framework enables the estimation of key wavelet parameters, including peak frequency, amplitude and phase, as well as the recovery of phase information and temporal positioning of wavelets (Zuniga et al. 2023b).

Each oscillatory component identified through the SR inversion is assigned a temporal position. These positions are stored in matrices in which columns correspond to seismic traces and rows correspond to detected wavelet events. The resulting matrices are used as input features for FCN training. Figure 5 illustrates the identification of SR-derived wavelet events and the assignment of their temporal positions within a representative seismic trace.

Reflection-event tracking across traces follows the methodology proposed by Zuniga and Priimenko (2024), in which wavelets are associated based on recovered spectral parameters. This procedure enables automatic identification of wavelets corresponding to the same reflection event within the seismic gather. The complete SR-based wavelet tracking and automated picking workflow is illustrated in Figure 6.

The tracking procedure requires an initial reference wavelet identified in the first trace. Subsequent wavelets are detected under three constraints: (1) monotonically increasing arrival times across traces; (2) intertrace time differences constrained within a predefined continuity window and (3) preservation of spectral similarity based on peak frequency, amplitude and phase.

The extracted spectral and temporal attributes are used as input features for the FCN model. The SR-based inversion relies primarily on relative spectral and temporal attributes, including peak frequency, phase and arrival time, reducing sensitivity to absolute amplitude scaling and preprocessing-related amplitude variations.

The SR-based feature extraction does not explicitly separate primary reflections, multiple-related events and diffracted wavefields. Consequently, the extracted spectral and temporal attributes represent the combined seismic response of the recorded wavefield, and multiple-related events and diffractions may contribute to the resulting FCN input features.

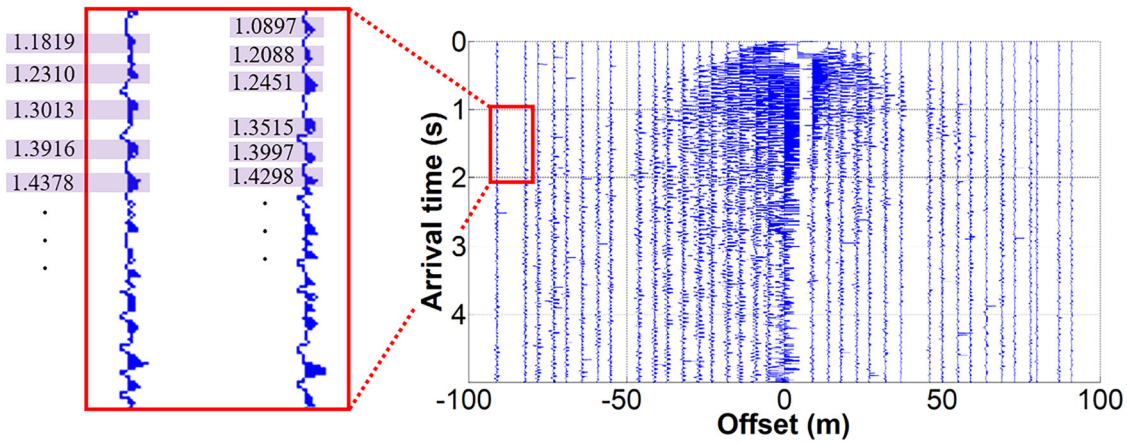

FIGURE 5 | Example of SR-based event identification in a seismic trace. A selected trace from the shot gather is highlighted and shown in detail. Individual wavelet events are identified within the trace (indicated by highlighted regions), and their corresponding arrival times are explicitly assigned. Each value represents the temporal position of a detected wavelet, illustrating how the SR time-position representation is constructed from the seismic signal.

3.4 | Dataset Construction and FCN Training

A total of 1000 training samples were generated, each consisting of an acoustic velocity model, corresponding synthetic seismic traces and SR-derived wavelet time-position matrices.

The synthetic models were constructed using near-surface velocity and thickness ranges reported for the Apollo missions. A representative conceptual set of near-surface models used to guide the SR–FCN training procedure is shown in Figure 7. Cooper et al. (1974) estimated a regolith layer with a P-wave velocity of approximately 100 m/s and thickness of about 4 m overlying a second layer with a velocity of 327 m/s and thickness of 32 m. Deeper structures at depths between approximately 250 and 370 m were reported by Heffels et al. (2021). Model parameters were randomized within these ranges to generate the synthetic dataset.

The forward-modelling grid consists of 201 × 301 spatial elements (horizontal distance × depth), with spatial sampling intervals of approximately 0.612 m horizontally and 0.503 m in depth. The seismic gathers and SR-derived feature matrices are represented in the time-offset domain with dimensions of 401 × 301 samples and used as FCN inputs. The FCN outputs velocity models with dimensions of 201 × 301 samples in the depth-horizontal domain.

After generating the synthetic gathers, the SR inversion was applied to estimate wavelet temporal positions. These estimates were stored as time-position matrices and paired with the corresponding seismic gathers and velocity models. The final training dataset, therefore, consists of triplets: (1) velocity model, (2) seismic combined CRG and (3) SR-derived wavelet time-position matrix, illustrated in Figure 8.

The network input consists of multi-channel SR-processed seismic traces, whereas the output corresponds to a pixel-wise velocity model. The dataset was divided into 80% training, 10% validation and 10% testing subsets.

The network input consists of five channels. The first channel corresponds to seismic amplitude data from the combined CRG, whereas the remaining four channels correspond to SR-derived wavelet time-position matrices. These matrices encode the temporal positions of multiple detected wavelet events across the seismic traces and are used as additional FCN input features.

The SR-derived features are incorporated through a scalar weighting factor γ, such that the multi-channel input tensor is defined as: $\mathbf{X} = [\mathbf{A}, \gamma\mathbf{T}_1, \gamma\mathbf{T}_2, \gamma\mathbf{T}_3, \gamma\mathbf{T}_4]$, where $\mathbf{A}$ represents the seismic amplitude data and $\mathbf{T}_i$ ($i = 1,\ldots,4$) denote the SR-derived wavelet time-position matrices. In this study, γ is treated as a fixed hyperparameter selected empirically prior to training to control the relative contribution of the SR-derived feature channels. Each channel is normalized prior to training to ensure numerical stability.

The FCN architecture follows an encoder–decoder structure inspired by Yang and Ma (2019) using an enhanced U-Net configuration, illustrated in Figure 9. The network includes successive convolutional layers with 64, 128, 256, 512 and 1024 feature channels, combined with max-pooling and transposed-convolution operations to capture multi-scale spatial features. Batch normalization is applied using the mean and standard deviation computed over each mini-batch, with a small constant ε added for numerical stability. A scalar weighting factor γ is introduced to control the relative contribution of the SR-derived feature channels during training.

Training was performed using the Adam optimizer with a learning rate of 10^{-4}, batch size of 8 and early stopping criteria. The loss function corresponds to the mean squared error (MSE) between predicted and reference velocity models. The network output is represented in the same spatial domain and resolution as the target velocity models, enabling direct pixel-wise comparison during training and evaluation.

Zero-padding is applied prior to convolutional operations to preserve spatial information and reduce boundary effects during feature extraction. Variations in feature-map dimensions result

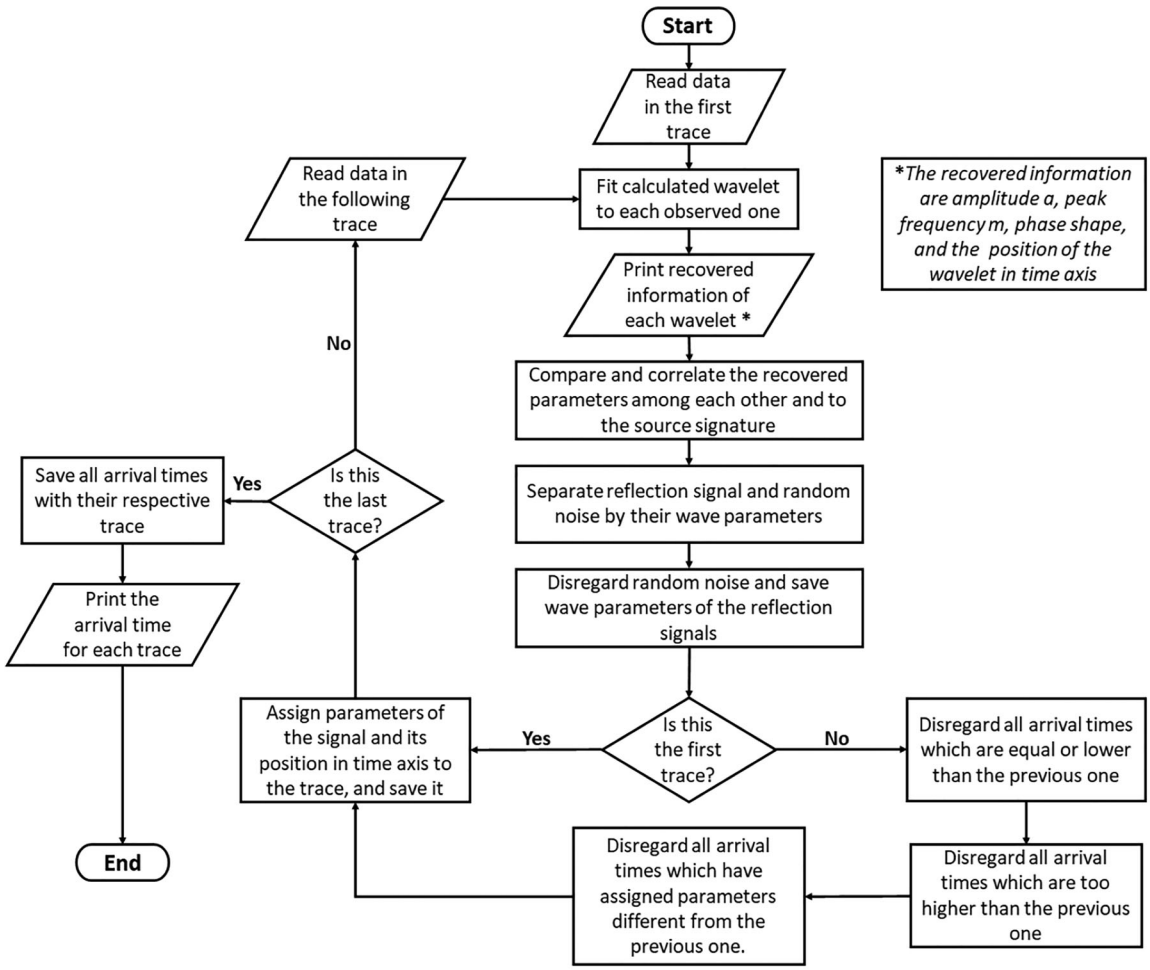

FIGURE 6 | Flowchart of the travel time automated picking algorithm through SR analyses (adapted from Zuniga and Priimenko 2024).

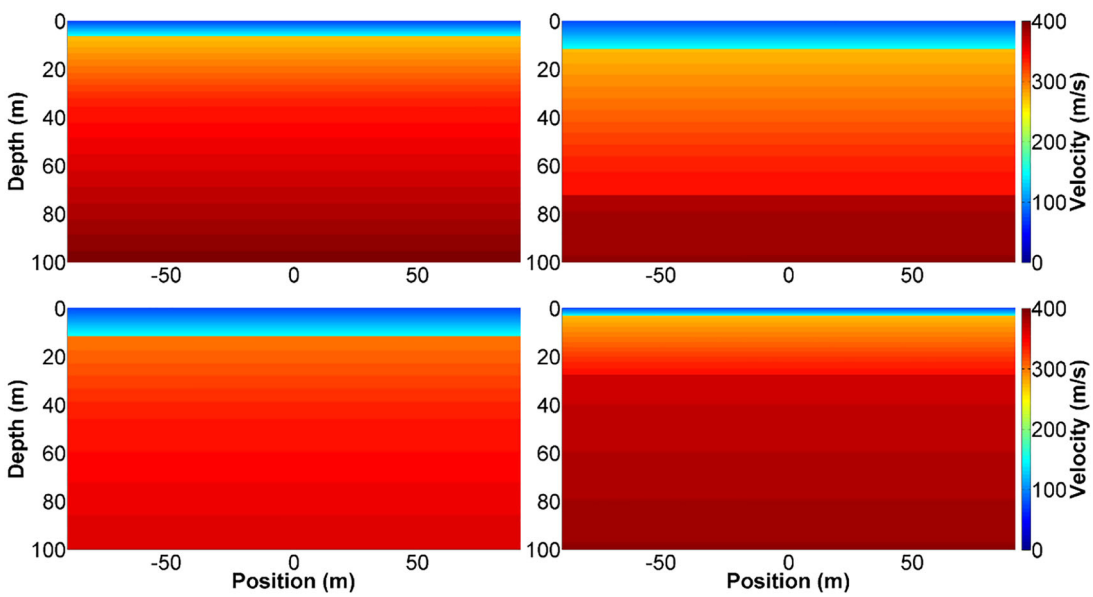

FIGURE 7 | Conceptual model of the Apollo 16 near-surface structure used for SR–FCN training and inversion. The sequence includes unconsolidated regolith (compressional velocity between 100 and 200 m/s) brecciated transition zone (compressional velocity between 250 and 350 m/s).

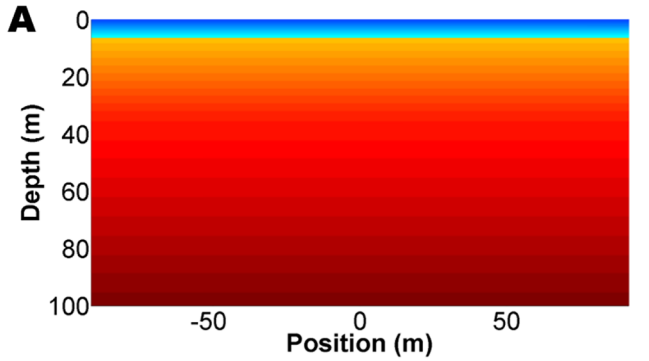

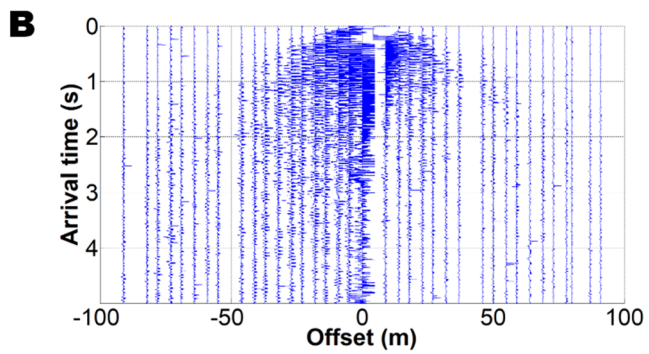

C

0.1025	0.1002	0.0981	0.0961	⋯
0.1032	0.1015	0.0992	0.0970	⋯
0.1043	0.1025	0.1001	0.0979	⋯
0.1056	0.1037	0.1012	0.0992	⋯
⋮	⋮	⋮	⋮	⋱

FIGURE 8 | Training set content showing (A) one of the acoustic velocity models, (B) the respective seismogram generated for the sources of a super gather with 37 receivers and (C) the respective matrix of the estimated position in time for each wavelet in the seismogram.

from the combined effects of padding, convolution, pooling and upsampling operations within the encoder–decoder architecture.

A key enhancement of the proposed framework is the incorporation of SR-derived wavelet time-position matrices as additional FCN input features (Zuniga 2024).

3.5 | Validation and Robustness Assessment

Model performance was evaluated using root-mean-square error (RMSE) and Jaccard similarity coefficient (JSC) (Liu et al. 2021; Gupta et al. 2022; Dong et al. 2024; Struble et al. 2020). The trained model was tested on synthetic data outside the training distribution and subsequently applied to the Apollo 16 dataset.

The RMSE quantifies the difference between the predicted model (**A**) and the ground truth (**G**) and is defined as

$$\mathrm{RMSE} = \sqrt{\frac{1}{MN}\sum_{i=1}^{N}\sum_{j=1}^{M}\left(u\left(i,j\right)-u_0\left(i,j\right)\right)^2}, \tag{5}$$

where $u(i, j)$ and $u_0(i, j)$ represent the predicted and reference values, respectively, M and N denote the horizontal and vertical model dimensions. RMSE ranges from 0 to ∞, where 0 indicates perfect agreement. Although RMSE measures the magnitude of prediction errors, it does not explicitly account for spatial structure or interface continuity.

The JSC measures the overlap between the ground truth (**G**) and the predicted model (**A**), ranging from 0 (no overlap) to 1 (perfect agreement) (Struble et al. 2020). It is defined as

$$\mathrm{JSC} = \frac{|\mathbf{G}\cap\mathbf{A}|}{|\mathbf{G}\cup\mathbf{A}|} = \frac{|\mathbf{G}\cap\mathbf{A}|}{|\mathbf{G}|+|\mathbf{A}|-|\mathbf{G}\cap\mathbf{A}|}. \tag{6}$$

Although RMSE quantifies the magnitude of prediction errors, JSC evaluates the spatial agreement between predicted and reference structures. However, JSC requires binarization, which may introduce thresholding effects.

4 | Results

Figure 10A shows the near-surface velocity estimation obtained from previous Apollo studies based on 1D models. To evaluate the impact of the SR-derived feature channels, conventional FCN training without the SR-derived matrices and weighting factor γ was also performed for comparison.

The prediction obtained using conventional FCN training (Figure 10B) reproduces the shallowest layers but shows limited resolution below approximately 60 m depth. In contrast, the SR–FCN prediction (Figure 10C) exhibits improved continuity of deeper interfaces and better delineation of shallow structures between approximately 9 and 30 m depth.

The predicted models in Figure 10B,C exhibit a well-defined shallow interface with localized lateral irregularities along the offsets. Quantitatively, the proposed SR–FCN approach achieved an RMSE of 0.0327 and a JSC of 0.6892, whereas the conventional FCN training resulted in an RMSE of 0.0492 and a JSC of 0.5185.

Apparent lateral velocity variations are observed in the predicted models. As the training dataset is based on laterally homogeneous models, these features should be interpreted with caution.

The predicted velocity models exhibit low-velocity shallow zones (100–200 m/s), intermediate velocity regions (250–350 m/s) and deeper high-velocity units (>350 m/s). A shallow low-velocity zone is observed between approximately 4 and 9 m depth, whereas denser layers are identified down to approximately 30 m depth. Deeper features extend to approximately 100 m depth, although resolution decreases with increasing depth due to acquisition limitations.

To further evaluate the physical consistency of the reconstructed velocity models, forward-modelling validation was performed using the predicted SR–FCN velocity field. Figure 11 compares the observed Apollo seismic gather (Figure 11A) with the synthetic gather (Figure 11B) generated under acquisition conditions consistent with the Apollo 16 experiment. The simulated data reproduce the main travel-time behaviour and reflected-event

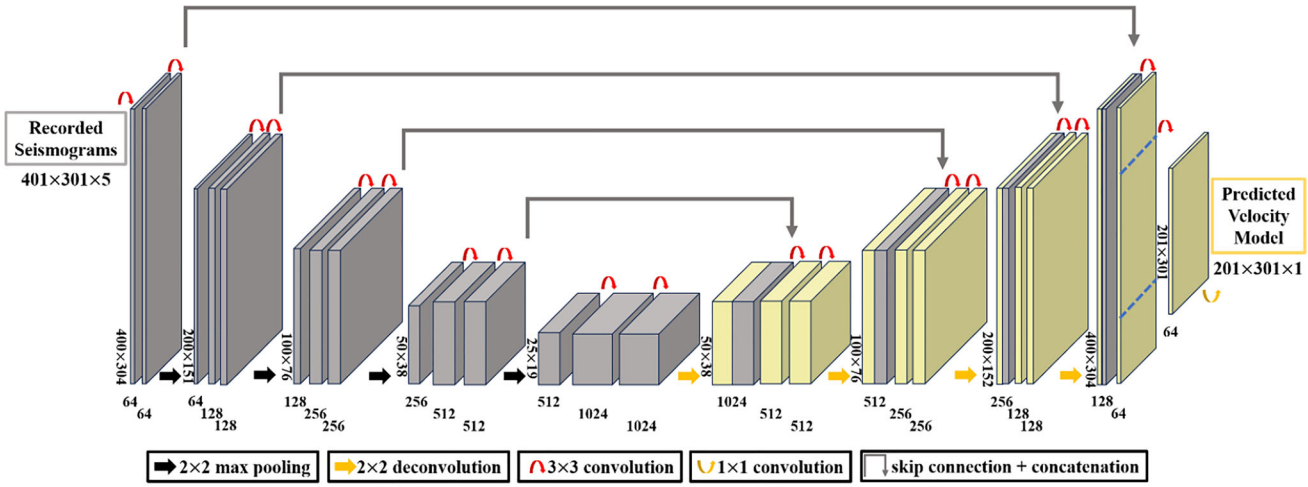

FIGURE 9 | NN architecture scheme used for this experiment. Each grey and yellow cube represents a multi-channel feature map. The number of channels is indicated below each cube. The x–z dimensions are shown at the lower left edge of each cube, and they refer to the spatial dimensions of the feature maps, corresponding to the horizontal (x) and vertical (depth, z) axes of the velocity model domain. Arrows indicate different operations, with the size of the corresponding parameter set specified inside each box (adapted from Yang and Ma 2019).

continuity observed in the field data. The residual section (Figure 11C) shows localized discrepancies, whereas the overall agreement supports the physical consistency of the reconstructed model. A normalized RMSE of 0.0617 was obtained between the observed and simulated seismograms.

5 | Discussion

The lunar near-surface is characterized by highly heterogeneous and unconsolidated materials, including dry regolith and fractured basaltic units, which strongly influence seismic wave propagation. The absence of fluid saturation and reduced attenuation conditions produce reflection patterns distinct from terrestrial environments. Although reduced attenuation improves temporal separation of seismic events, it also alters signal characteristics and must be considered during interpretation. In addition, the Apollo 16 ASE presents important acquisition limitations, including restricted offset range, sparse spatial sampling and low dynamic range associated with 5-bit digitization (NASA TM X-58131), making conventional inversion approaches difficult to apply.

To address these limitations, the SR stage plays a central role in the proposed workflow. Previous studies demonstrated the ability of SR-based approaches to improve spectral characterization under degraded acquisition conditions (Zuniga et al. 2023a, 2023b). This is particularly important for the Apollo dataset, which contains quantization noise, thermal drift and amplitude clipping. In this study, SR acts both as a feature-extraction and signal-enhancement step, enabling more stable estimation of wavelet parameters for FCN training.

The integration of SR-derived features into the FCN framework improves the integration of spectral and temporal information into the inversion process. Compared with conventional FCN training, the SR–FCN workflow produced improved continuity of deeper interfaces and reduced velocity smearing, as observed in Figure 10. Similar improvements in prediction stability and reconstruction accuracy were previously reported in SR-enhanced FCN studies (Zuniga 2024, 2026a).

It is important to emphasize that the lateral variations observed in the predicted velocity models are not directly constrained by the training dataset, which is based on laterally homogeneous (1D) models. Therefore, these variations should not be interpreted as direct evidence of true geological heterogeneity. Instead, they arise from the network's response to variations in the seismic input, including acquisition geometry, wave propagation effects and noise characteristics. As a result, they may reflect underlying physical relationships, although they are also influenced by data limitations and the learning process.

The predicted velocity ranges and shallow-layer thicknesses are broadly consistent with values reported in previous Apollo studies (Cooper et al. 1974; Sens-Schönfelder and Larose, 2010; Heffels et al. 2021). In particular, the shallow low-velocity zone identified between approximately 4 and 9 m depth falls within the range commonly associated with the lunar regolith. Although some localized anomalies may be consistent with fractured or brecciated regions in the lunar near-surface, their spatial distribution cannot be independently validated within the scope of this study. These localized features are illustrated in Figure 12.

Despite these improvements, the method presents limitations in resolving deeper structures beyond approximately 100 m depth, primarily due to the restricted offset range of the Apollo 16 experiment. Extending the acquisition geometry would likely improve depth penetration and model reliability.

In addition, the SR-based feature extraction does not explicitly distinguish between primary reflection events, multiple-related events and diffracted wavefields. These wave phenomena are incorporated together within the extracted attributes and may influence both the spectral representation and the FCN predictions.

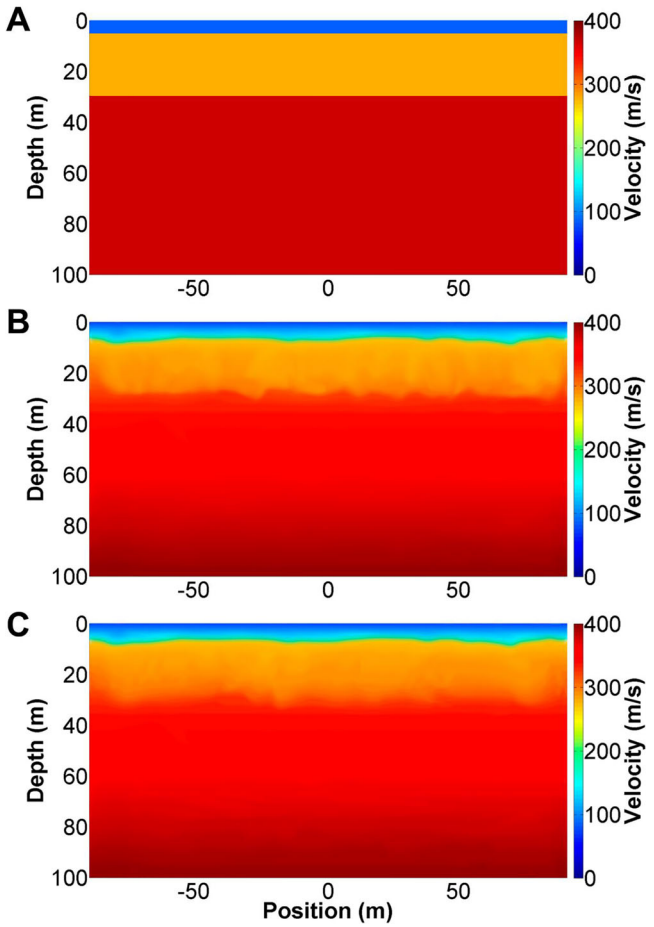

FIGURE 10 | Comparison of near-surface velocity models obtained using different inversion approaches. (A) Prediction based on 1D velocity profiles from previous studies of the Apollo 16 site, showing a simple regolith–megaregolith boundary. (B) FCN prediction result using conventional training without spectral features, where layer boundaries appear diffuse. (C) FCN prediction results trained with spectral-recomposition features, revealing improved delineation of the regolith, brecciated transition zone.

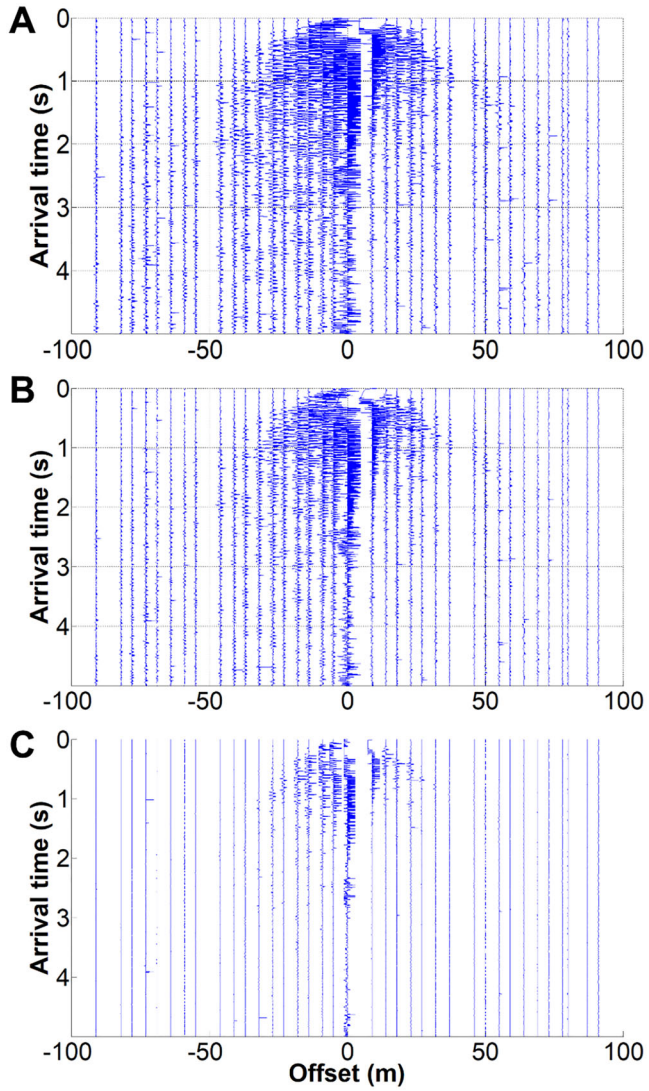

FIGURE 11 | Comparison between observed and forward-modelled seismic data. (A) Observed Apollo 16 seismic gather. (B) Synthetic gather generated through forward modelling using the predicted velocity model obtained from the SR–FCN workflow. (C) Residual between observed and simulated seismograms (observed synthetic), highlighting localized discrepancies. The overall agreement in travel-time behaviour and event continuity, together with relatively low residual amplitudes, indicates that the reconstructed velocity model is physically consistent with the observed seismic response.

The results presented in this study are also limited by the two-dimensional approximation imposed by the linear acquisition geometry of the Apollo 16 experiment. Although this configuration allows reconstruction of laterally varying structures along the profile, it does not account for out-of-plane heterogeneities inherent to the lunar subsurface.

Additional uncertainty may arise from preprocessing choices and from the idealized Ricker-wavelet assumption adopted in the SR decomposition. Filtering, spectral balancing, instrument response, attenuation and digitization effects may influence the recovered spectral attributes and consequently affect the FCN inputs and predictions.

The proposed workflow offers important computational advantages by avoiding global optimization procedures. Instead, the use of multi-start local-search optimization (Sotirov and Terlaky 2013) enables efficient estimation of wavelet parameters while maintaining stable inversion performance.

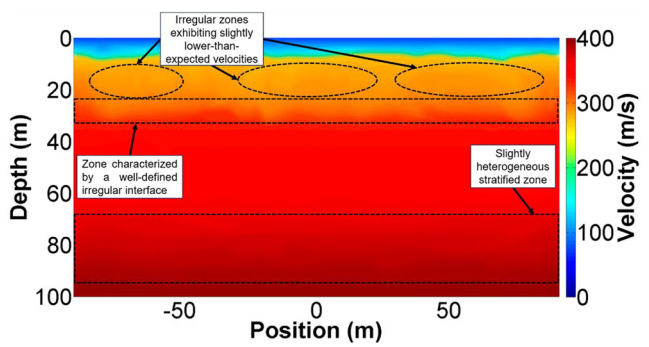

FIGURE 12 | Annotated view of the SR–FCN velocity prediction highlighting reconstructed spatial variability within the shallow lunar subsurface under the acquisition constraints of the Apollo 16 dataset.

Given the inherent non-uniqueness of seismic inversion under limited acquisition conditions, approaches that integrate physical constraints with data-driven methods, such as the SR–FCN workflow, are important for producing geophysically consistent results from degraded lunar seismic datasets.

Overall, the proposed method provides a robust framework for reanalysing legacy lunar seismic data and provides a useful framework for future lunar exploration, including site characterization, subsurface stability assessment and resource exploration.

6 | Conclusions

We proposed an alternative workflow for near-surface seismic analysis of the Moon based on SR and FCNs. The proposed approach uses wavelet-based SR inversion to extract spectral and temporal attributes, including time position, peak frequency, amplitude and phase, which are incorporated as structured input features for FCN-based velocity prediction. Compared with conventional FCN training, the SR–FCN workflow produced improved continuity of deeper interfaces and reduced velocity smearing in the reconstructed lunar near-surface models.

The predicted velocity structures are broadly consistent with previously reported Apollo near-surface properties, although the observed lateral variability should be interpreted with caution due to acquisition limitations and the use of laterally homogeneous training models. Despite these limitations, the results demonstrate that the proposed workflow can recover coherent subsurface information from degraded lunar seismic data acquired under restricted acquisition conditions.

Overall, the proposed methodology provides a robust and computationally efficient framework for reanalysing legacy lunar seismic datasets and offers relevant perspectives for future lunar exploration, including near-surface characterization, subsurface stability assessment and resource exploration.

Acknowledgements

The authors acknowledge the support of the Laboratório de Modelagem e Simulação, Instituto do Mar, Universidade Federal de São Paulo. The first author also acknowledges financial support from the Fundação de Amparo à Pesquisa do Estado de São Paulo (FAPESP) through Regular Research Grant No. 2024/18458-8.

The Article Processing Charge for the publication of this research was funded by the Coordenação de Aperfeiçoamento de Pessoal de Nível Superior - Brasil (CAPES) (ROR identifier: 00x0ma614).

Data Availability Statement

The Apollo seismic data and moon's site location used in this study are available through the NASA National Space Science Data Center (NSSDC), as described in the original mission documentation (NASA TM X-58131).

References

Adler, A., M. Araya-Polo, and T. Poggio. 2021. "Deep Learning for Seismic Inverse Problems: Toward the Acceleration of Geophysical Analysis Workflows." *IEEE Signal Processing Magazine* 38: 89–119.

An, Y., J. Guo, Q. Ye, C. Childs, J. Walsh, and R. Dong. 2021. "Deep Convolutional Neural Network for Automatic Fault Recognition From 3D Seismic Datasets." *Computers & Geosciences* 153: 104776.

Cai, Y., S. Fomel, and H. Zeng. 2013. "Automated Spectral Recomposition With Application in Stratigraphic Interpretation." *Interpretation* 1, no. 1: SA109–SA116.

Castagna, J. P., S. Sun, and R. W. Siegfried. 2003. "Instantaneous Spectral Analysis: Detection of Low-Frequency Shadows Associated With Hydrocarbons." *Leading Edge* 22: 120–127.

Cooper, M. R., R. L. Kovach, and J. S. Watkins. 1974. "Lunar Near-Surface Structure." *Reviews of Geophysics* 12, no. 3: 291–308.

Di, H., D. Gao, and G. AlRegib. 2019. "Developing a Seismic Texture Analysis Neural Network for Machine-Aided Seismic Pattern Recognition and Classification." *Geophysical Journal International* 218, no. 2: 1262–1275.

Dong, X., C. Wei, T. Zhong, M. Cheng, S. Dong, and F. Li. 2024. "Seismic Data Reconstruction Based on a Multicascade Self-Guided Network." *Geophysics* 89, no. 3: V179–V195.

Gammaldi, S., A. Ismail, and A. Zollo. 2022. "Fluid Accumulation Zone Inferred by Seismic Attributes and Amplitude Versus Offset Analysis at the Solfatara Volcano, Campi Flegrei, Italy." *Frontiers in Earth Science* 10: 866534.

Gupta, D., U. Kose, A. Khanna, and V. E. Balas. 2022. *Deep Learning for Medical Applications With Unique Data*. Academic Press.

Heffels, A., M. Knapmeyer, J. Oberst, and I. Haase. 2021. "Re-Evaluation of Apollo 17 Lunar Seismic Profiling Experiment Data Including New LROC-Derived Coordinates for Explosive Packages 1 and 7, at Taurus-Littrow, Moon." *Planetary and Space Science* 206: 105307.

Huang, N. E., Z. Shen, S. R. Long, et al. 1998. "The Empirical Mode Decomposition and the Hilbert Spectrum for Nonlinear and Non-Stationary Time Series Analysis." *Proceedings of the Royal Society A* 454, no. 1971: 903–995.

Imazato, H., T. Ikeda, and T. Tsuji. 2023. "Shallow S-Wave Velocity Profile From Active-Source Seismic Data at the Apollo 14 Landing Site Based on Virtual Multichannel Analysis of Surface Waves." *Icarus* 406: 115 724.

Ismail, A., H. F. Ewida, M. G. Al-Ibiary, and A. Zollo. 2020. "Integrated Prediction of Deep-Water Gas Channels Using Seismic Coloured Inversion and Spectral Decomposition Attribute, West Offshore, Nile Delta, Egypt." *NRIAG Journal of Astronomy and Geophysics* 9, no. 1: 459–470.

Ismail, A., H. F. Ewida, M. G. Al-Ibiary, et al. 2021. "The Detection of Deep Seafloor Pockmarks, Gas Chimneys, and Associated Features With Seafloor Seeps Using Seismic Attributes in the West Offshore Nile Delta, Egypt." *Exploration Geophysics* 52, no. 4: 388–408.

Ismail, A., H. F. Ewida, S. Nazeri, M. G. Al-Ibiary, and A. Zollo. 2022. "Gas Channels and Chimneys Prediction Using Artificial Neural Networks and Multi-Seismic Attributes, Offshore West Nile Delta, Egypt." *Journal of Petroleum Science and Engineering* 208: 109349.

Jia, Y., and J. Ma. 2017. "What Can Machine Learning Do for Seismic Data Processing? An Interpolation Application." *Geophysics* 82, no. 3: V163–V177.

Jia, Y., S. Yu, and J. Ma. 2018. "Intelligent Interpolation by Monte Carlo Machine Learning." *Geophysics* 83, no. 2: V83–V97.

Klochikhina, E., S. Crawley, S. Frolov, N. Chemingui, and T. Martin. 2020. "Leveraging Deep Learning for Seismic Image Denoising." *First Break* 38: 41–48.

Larose, E., A. Khan, Y. Nakamura, and M. Campillo. 2005. "Lunar Subsurface Investigated From Correlation of Seismic Noise." *Geophysical Research Letters* 32: L16201.

Li, Y., X. Zheng, and Y. Zhang. 2011. "High-Frequency Anomalies in Carbonate Reservoir Characterization Using Spectral Decomposition." *Geophysics* 76: V47–V57.

Li, S., C. Yang, H. Sun, and H. Zhang. 2019. "Seismic Fault Detection Using an Encoder–Decoder Convolutional Neural Network With a Small Training Set." *Journal of Geophysics and Engineering* 16, no. 5: 175–189.

Liu, B., S. Yang, Y. Ren, X. Xu, P. Jiang, and Y. Chen. 2021. "Deep-Learning Seismic Full-Waveform Inversion for Realistic Structural Models." *Geophysics* 86, no. 1: R31–R44.

NASA. 1974. *Apollo Scientific Experiments Data Handbook*. JSC-09166 NASA TM X-58131. NASA.

Nishitsuji, Y., C. A. Rowe, K. Wapenaar, and D. Draganov. 2016. "Reflection Imaging of the Moon's Interior Using Deep-Moonquake Seismic Interferometry." *Journal of Geophysical Research: Planets* 121: 695–713.

Nishitsuji, Y., E. Ruigrok, and D. Draganov. 2020. "Azimuthal Anisotropy of the Megaregolith at the Apollo 14 Landing Site." *Journal of Geophysical Research: Planets* 125: 1–16.

Ren, Y., X. Xu, S. Yang, L. Nie, and Y. Chen. 2020. "A Physics-Based Neural-Network Way to Perform Seismic Full-Waveform Inversion." *IEEE Access* 8: 112266–112277.

Ricker, N. 1953. "The Form and Laws of Propagation of Seismic Wavelets." *Geophysics* 18: 10–40.

Ronneberger, O., P. Fischer, and T. Brox. 2015. "U-Net: Convolutional Networks for Biomedical Image Segmentation." In N. Navab, J. Hornegger, W. Wells, A. Frangi (eds) *Medical Image Computing and Computer-Assisted Intervention MICCAI 2015. MICCAI 2015. Lecture Notes in Computer Science*, 9351. Springer, Cham. https://doi.org/10.1007/978-3-319-24574-4_28.

Sens-Schönfelder, C., and E. Larose. 2010. "Lunar Noise Correlation, Imaging and Monitoring." *Earthquake Science* 23: 519–530.

Struble, W. T., J. J. Roering, R. J. Dorsey, and R. Bendick. 2020. "Characteristic Scales of Drainage Reorganization in Cascadia." *Geophysical Research Letters* 48: e2020GL089326.

Sotirov, R., and T. Terlaky. 2013. "Multi-Start Approach for an Integer Determinant Maximization Problem." *Optimization* 62: 101–114.

Thorbecke, J., and D. Draganov. 2011. "Finite-Difference Modeling Experiments for Seismic Interferometry." *Geophysics* 76: H1–H18.

Tomasso, M., R. Bouroullec, and D. R. Pyles. 2010. "The Use of Spectral Recomposition in Tailored Forward Seismic Modeling of Outcrop Analogs." *AAPG Bulletin* 94, no. 4: 457–474.

Wood, L. C. 1974. "Seismic Data Compression Methods." *Geophysics* 39, no. 4: 499–525.

Wrona, T., I. Pan, R. L. Gawthorpe, and H. Fossen. 2018. "Seismic Facies Analysis Using Machine Learning." *Geophysics* 83, no. 5: O83–O95.

Yang, F., and J. Ma. 2019. "Deep-Learning Inversion: a Next-Generation Seismic Velocity Model Building Method." *Geophysics* 84, no. 4: R583–R599.

Zhang, M., Y. Liu, and Y. Chen. 2019. "Unsupervised Seismic Random Noise Attenuation Based on Deep Convolutional Neural Network." *IEEE Access* 7: 179810–179822.

Zuniga, N. R. C. F. 2024. "Spectral Recomposition Feature for Optimizing Seismic Velocity Model Prediction With a Neural Network." *Journal of Applied Geophysics* 226: 105411.

Zuniga, N. R. C. F. 2026a. "Optimizing Downdip Interface Prediction by Using Seismic Features for Training a Neural Network." *Petroleum Geoscience* 32: 1–20.

Zuniga, N. R. C. F. 2026b. "Neural network with signal parameters featuring for near-surface velocity model building." *Near Surface Geophysics* 24: 289–299.

Zuniga, N. R. C. F., and V. I. Priimenko. 2024. "Inversion Procedure for Velocity Analysis Using Spectral Recomposition." *Marine Geophysical Research* 45, no. 4: 1–13.

Zuniga, N. R. C. F., and V. I. Priimenko. 2025. "Inversion of Signal Parameters Through Spectral Recomposition: Geosciences Applications." *Eurasian Journal of Mathematical and Computer Applications* 13: 169–183.

Zuniga, N. R. C. F., D. Draganov, and R. Ghose. 2023a. "Critical Angle of Reflections and Poisson's Ratio From Spectral Recomposition." *Journal of Applied Geophysics* 215: 105110.

Zuniga, N. R. C. F., D. Draganov, and R. Ghose. 2023b. "Phase-shift Correction of Seismic Reflections by Means of Spectral Recomposition." *Near Surface Geophysics* 21: 414–426.